Journal of Colloid and Interface Science 634 (2023) 323–335

Contents lists available at ScienceDirect

Journal of Colloid and Interface Science

journal homepage: www.elsevier.com/locate/jcis

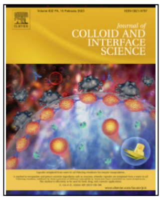

“Non-cytotoxic” doses of metal-organic framework nanoparticles increase endothelial permeability by inducing actin reorganization

Jinyuan Liu [a,c], Alex Rickel [b,c], Steve Smith [a,c], Zhongkui Hong [b,c,d,*], Congzhou Wang [a,c,*]

[a] Nanoscience and Nanoengineering, South Dakota School of Mines and Technology, 501 East Saint Joseph Street, Rapid City, SD 57701, USA
[b] Biomedical Engineering, University of South Dakota, 4800 N Career Avenue, Sioux Falls, SD 57107, USA
[c] BioSystems, Networks & Translational Research (BioSNTR), 501 East Saint Joseph Street, Rapid City, SD 57701, USA
[d] Mechanical Engineering, Texas Tech University, 805 Boston Ave, Lubbock, TX 79409, USA

GRAPHICAL ABSTRACT

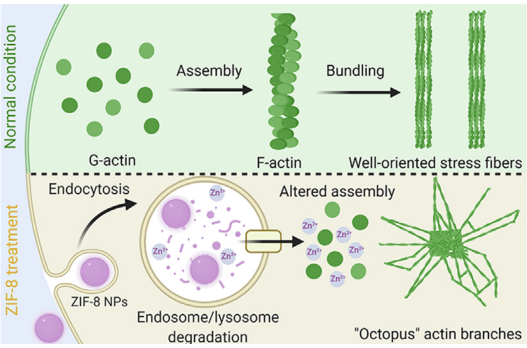

ARTICLE INFO

Article history:
Received 27 October 2022
Revised 28 November 2022
Accepted 5 December 2022
Available online 9 December 2022

Keywords:
Zeolitic imidazolate framework-8 nanoparticles
Human aortic endothelial cells
Non-cytotoxic doses
Endothelial permeability
Actin reorganization

ABSTRACT

Cytotoxicity of nanoparticles is routinely characterized by biochemical assays such as cell viability and membrane integrity assays. However, these approaches overlook cellular biophysical properties including changes in the actin cytoskeleton, cell stiffness, and cell morphology, particularly when cells are exposed to “non-cytotoxic” doses of nanoparticles. Zeolitic imidazolate framework-8 nanoparticles (ZIF-8 NPs), a member of metal–organic framework family, has received increasing interest in various fields such as environmental and biomedical sciences. ZIF-8 NPs may enter the blood circulation system after unintended oral and inhalational exposure or intended intravenous injection for diagnostic and therapeutic applications, yet the effect of ZIF-8 NPs on vascular endothelial cells is not well understood. Here, the biophysical impact of “non-cytotoxic” dose ZIF-8 NPs on human aortic endothelial cells (HAECs) is investigated. We demonstrate that “non-cytotoxic” doses of ZIF-8 NPs, pre-defined by a series of biochemical assays, can increase the endothelial permeability of HAEC monolayers by causing cell junction disruption and intercellular gap formation, which can be attributed to actin reorganization within adjacent HAECs. Nanomechanical atomic force microscopy and super resolution fluorescence microscopy further confirm that “non-cytotoxic” doses of ZIF-8 NPs change the actin structure and cell morphology of HAECs at the single cell level. Finally, the underlying mechanism of actin reorganization induced by the “non-cytotoxic” dose ZIF-8 NPs is elucidated. Together, this study indicates that the “non-cytotoxic” doses of ZIF-8 NPs, intentionally or unintentionally introduced into blood circulation, may still pose a threat to human health, considering increased endothelial permeability is essential to the progression of a variety of diseases. From a broad view of cytotoxicity evaluation, it is important to consider the

---

[*] Corresponding authors at: BioSystems, Networks & Translational Research (BioSNTR), 501 East Saint Joseph Street, Rapid City, SD 57701, USA.
E-mail addresses: zhongkui.hong@ttu.edu (Z. Hong), congzhou.wang@sdsmt.edu (C. Wang).

https://doi.org/10.1016/j.jcis.2022.12.020

biophysical properties of cells, since they can serve as novel and more sensitive markers to assess nanomaterial's cytotoxicity.

1. Introduction

"The dose makes the poison." This adage by Paracelsus describes that the administered dose of a substance is a fundamental parameter that determines its toxicity [1]. Likewise, cellular uptake of nanoparticles induces dose-dependent detrimental effects on cells, which are routinely characterized by biochemical cytotoxicity assays [2–3]. Among these, cell viability (e.g., MTT) and membrane integrity (e.g., lactate dehydrogenase, LDH) assays are the most-used biochemical assays for evaluating nanoparticle cytotoxicity [4–5]. Typically, nanoparticle doses that cause obvious changes in cell viability and membrane integrity are considered as "cytotoxic" or "harmful" doses at the *in vitro* level, implying that the nanoparticles should not be harmful to cells below these "cytotoxic" doses. However, these assays used to define "cytotoxic" doses neglect the cellular biophysical changes that nanoparticles can cause, such as alterations of the actin cytoskeleton, cell stiffness, and cell morphology.[6–8] Indeed, the majority of previous research assumes these biophysical changes are the consequences of reduced cell viability and membrane integrity, when cells are exposed to "cytotoxic" nanoparticles.[9–11] However, recent studies suggested that before reaching a certain "cytotoxic" dose as defined by biomedical assays, these biophysical changes have already taken place on cells.[12–13] For instance, a pioneering study by Liang, Parak, and co-authors found that the actin cytoskeleton and cell morphology can be affected by gold nanoparticles, under "non-cytotoxic" doses when cell viability and membrane integrity have not yet been changed.[12] Another study by Leong's group also demonstrated that TiO_2 nanoparticles altered the morphology of cancer cells and thus increased their migration ability after exposure to "non-cytotoxic" doses of nanoparticles.[13] Together, the following questions arise: Are the "non-cytotoxic" doses really "non-harmful" to cells, and how will these so-called "non-cytotoxic" doses of nanoparticles affect cells in terms of their often-overlooked biophysical properties?

Metal-organic frameworks (MOFs), a class of hybrid crystalline materials formed by coordination bonds between metal ions and organic linkers, have shown great promise in a variety of environmental and biomedical applications, such as biosensing,[14–18] bioimaging,[19–23] bio-preservation,[24–27] drug delivery,[28–32] photodynamic therapy,[33–34] and immunotherapy.[35] As an important member of MOF family, zeolitic imidazolate framework-8 nanoparticles (ZIF-8 NPs), consisting of zinc ions and 2-methylimidazole, have been extensively utilized to encapsulate and deliver drug molecules for treating diseases,[36–38] owing to their high drug loading efficacy, mild drug loading condition, and responsive drug release in acidic pH.[39–42] This is also because ZIF-8 is typically recognized as a biocompatible material with relatively low cytotoxicity since both zinc and the imidazole group are abundant in cellular systems.[43] To date, the cytotoxicity of ZIF-8 NPs has been assessed using conventional biochemical assays on a broad range of mammalian cells including cancer cells, macrophages, epithelial cells, and fibroblasts.[43–45] However, there is still missing information about how ZIF-8 NPs interact with vascular endothelial cells, the cell monolayer that forms the interior surfaces of blood vessels. Considering contact of ZIF-8 NPs with vascular endothelial cells can occur due to the translocation of the NPs into blood circulation after unintended oral and inhalational exposure, or intended intravenous injection for biomedical applications,[46–49] it is of great importance to understand the impact of ZIF-8 NPs on vascular endothelial cells.

In this work, we investigated whether and how the "non-cytotoxic" doses of ZIF-8 NPs affect the biophysical properties of vascular endothelial cells. Human aortic endothelial cells (HAECs) were selected as our endothelial cell model since they are widely used to study endothelial dysfunction and cardiovascular diseases caused by air pollution, oxidative stress, inflammation, and nanomaterial exposure.[50–53] First, we identified the "non-cytotoxic" doses of ZIF-8 NPs on HAECs using a series of biochemical assays. Next, we evaluated the effect of "non-cytotoxic" doses of ZIF-8 NPs on the endothelial integrity and permeability, considering the main function of endothelial cells is to maintain the vascular homeostasis *via* regulating the transport of macromolecules, circulating cells, and nanomedicines between tissues and the bloodstream.[54–55] We found the confluent HAEC monolayer, after treatment with these "non-cytotoxic" doses of ZIF-8 NPs, showed significantly increased permeability by forming micrometer-sized gaps between adjacent cells. We further examined the ZIF-8 nanoparticle-treated HAECs at the single cell level by atomic force microscopy and super resolution fluorescence microscopy, and demonstrated that ZIF-8 NPs, even at "non-cytotoxic" doses, changed the actin cytoskeleton and morphology of HAECs, resulting in a disruption to the cell junction and an increase in the endothelial permeability. Finally, we elucidated the underlying mechanism of how "non-cytotoxic" dose ZIF-8 NPs induced structural changes in the actin cytoskeleton of HAECs. Together, this work provides an important safety guideline for *in vivo* applications of ZIF-8 NPs (e.g., intravenous injection for drug delivery), given that even "non-cytotoxic" doses of ZIF-8 NPs have the potential to cause endothelial dysfunction and increase the risk of cardiovascular diseases. From the broad point view of nanotoxicity evaluation, the cellular biophysical characteristics offer novel and more sensitive indicators to assess nanoparticle induced cytotoxicity.

2. Results and discussion

2.1. Characterization and cytotoxicity of ZIF-8 NPs

ZIF-8 NPs were synthesized using an established protocol,[45] which led to monodispersed nanospheres with an average diameter of 63.4 ± 9.7 nm, as shown in transmission electron microscope images (Fig. 1A and S1). This size falls into the optimal size range of nanoparticles for cellular uptake.[56] All of the diffraction peaks associated with a standard ZIF-8 crystal structure were visible in powder X-ray diffraction of synthesized ZIF-8 NPs, indicating the formation of ZIF-8 crystalline NPs (Fig. 1B).[57] The colloidal stability of ZIF-8 NPs in aqueous media were characterized using dynamic light scattering (DLS). The hydrodynamic size of ZIF-8 NPs in PBS buffer was measured to be 66.3 nm (PDI: 0.114), and the size slightly increased to 69.4 nm (PDI: 0.179) in cell culture medium due to the formation of protein corona on the nanoparticle surface (Fig. 1C). The formation of protein corona was confirmed by the SDS-PAGE experiment, suggesting that a series of serum proteins adsorbed on the nanoparticle surface, where the strongest band corresponds to the most abundant albumin in serum (**Figure S2**). There was no significant change in the hydrodynamic size after incubating with cell culture medium for 24 h,

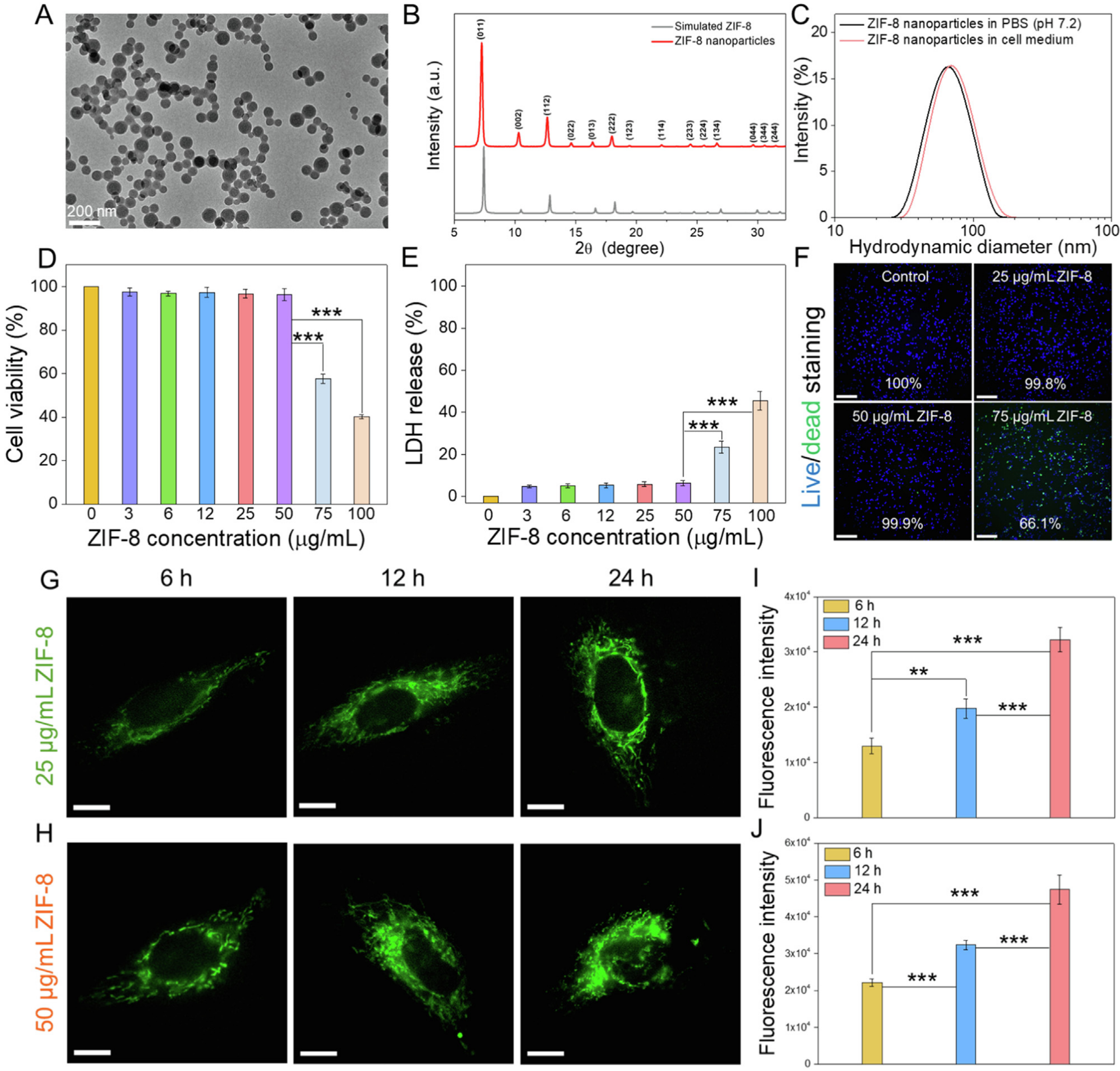

Fig. 1. Characterization, cytotoxicity, and HAEC uptake of ZIF-8 NPs. (A) Representative TEM image of ZIF-8 NPs. (B) Powder XRD pattern of synthesized and simulated ZIF-8. (C) Hydrodynamic diameter of ZIF-8 NPs in aqueous media. For ZIF-8 NPs in PBS, the peak size is 66.3 nm and the PDI is 0.114. For ZIF-8 NPs in cell medium, the peak size is 69.4 nm, and PDI is 0.179. (D-F) Biochemical-based cytotoxicity assays (D: XTT assay, E: LDH assay, F: live/dead staining) evaluating dose-dependent effect of ZIF-8 NPs on HAECs. Scale bars: 200 μm. Data are mean ± SD, n = 6. One-way ANOVA test, $***P < 0.001$. (G-H) Fluorescence images of individual HAECs after cell incubation with 25 and 50 μg/mL of FITC@ZIF-8 NPs for 6, 12, and 24 h. Scale bars: 10 μm. (I-J) Quantitative analysis of correlated total cell fluorescence of 25 and 50 μg/mL FITC@ZIF-8 NPs treated HAECs. Data are mean ± SD, n = 10. One-way ANOVA test, $**P < 0.01$, $***P < 0.001$.

indicating good colloidal stability of ZIF-8 NPs in the physiological fluid within a short term (**Figure S3**). The powder X-ray diffraction of ZIF-8 NPs after incubation with cell medium for 24 h maintained all the diffraction peaks of freshly prepared ZIF-8 NPs, with three additional peaks at 10.968°, 18.912°, and 23.912°, consistent with previous reported data,[58] suggesting good chemical stability of ZIF-8 NPs in the physiological fluid within a short term (**Figure S4**).

The cytotoxicity of ZIF-8 NPs on human aortic endothelial cells (HAECs) was evaluated through three commonly used biochemical assays, including an XTT, a LDH, and a live/dead staining assay. The XTT assay assesses cell viability by measuring cellular metabolic activity, whereas the LDH assay determines cell membrane damage by quantifying the leaked cytosolic enzyme, lactate dehydrogenase (LDH).[59–60] As a combination and complement of XTT and LDH assays, live/dead staining assay determines cell viability by counting total versus membrane-compromised dead cells. As depicted in Fig. 1D-1F, the cell viability and membrane integrity of HAECs after incubation with ZIF-8 NPs for 24 h manifested a dose-dependent manner. The HAECs maintained over 90 % viability after being treated with lower concentrations of ZIF-8 NPs (≤50 μg/mL), whereas the cell viability dropped significantly to 57 % and 40 % when ZIF-8 nanoparticle doses increased to 75 and 100 μg/mL, respectively. A similar trend was noticeable on the membrane integrity: Lower doses of ZIF-8 NPs (≤50 μg/mL) caused negligible membrane damage, while doses higher than 50 μg/mL (i.e., 75 and 100 μg/mL) led to significant LDH leakage, suggesting the membrane damage after the nanoparticle treatments. Together, the two biochemical assays identified a non-cytotoxic to cytotoxic threshold for ZIF-8 NPs on HAECs, centered around 50 μg/mL. In other words, the doses no higher than 50 μg/mL could be considered as "safe" or "non-cytotoxic" doses, which was further reinforced by the live/dead staining assay (Fig. 1F and S5). In the following experiments, we selected the doses of 25 and 50 μg/mL to assess the effects of presumably "safe" doses of ZIF-8 NPs on HAECs.

2.2. HAEC uptake of ZIF-8 NPs

To investigate the uptake of ZIF-8 NPs by HAECs, a small molecular dye, fluorescein isothiocyanate (FITC), was loaded into ZIF-8 NPs during synthesis to generate fluorescence-labelled ZIF-8 NPs (i.e., FITC@ZIF-8 NPs).[45] FITC@ZIF-8 NPs can emit green fluorescence under excitation and the internalized amounts of ZIF-8 NPs by cells can be determined using a quantitative method established in our group, namely, correlated total cell fluorescence (CTCF).[61] Fig. 1G-1J and S6-S7 show that ZIF-8 NPs are internalized by HAECs in a dose- and time-dependent fashion. As incubation time and nanoparticle dose increase, HAECs exhibited increased fluorescence intensity across the entire cells except the cellular nuclei, suggesting that ZIF-8 NPs were indeed internalized by HAECs, instead of adhering on the cell surface. This was further confirmed by the presence of fluorescent intracellular vesicles (i.e., the isolated green dots, Fig. 1G and 1H), suggesting that the nanoparticles were likely accumulated within the endosome/lysosome after endocytosis.[62] As a control experiment, incubating HAECs with free FITC in cell medium for 24 h only produced minimal CTCF (**Figure S8**). The cellular uptake of nanoparticles was found to be largely through a caveolae-mediated pathway as pretreating the HAECs with methyl-β-cyclodextrin (an inhibitor for caveolae-mediated endocytosis) significantly reduced the cellular uptake of nanoparticles (**Figure S8**). Through the fluorescence images, we also noticed that the HAECs gradually changed their morphology within the 24 h incubation period, during which the cell shape became rounded as manifested by a reduced aspect ratio of individual cells (**Figure S9**). These results demonstrate the time- and dose-dependent HAEC uptake of ZIF-8 NPs, along with the morphological change of HAECs induced by the "non-cytotoxic" dose ZIF-8 NPs.

2.3. Cellular uptake of ZIF-8 NPs increases endothelial permeability of HAECs

Considering the morphology of endothelial cells is pivotal to the endothelial barrier function,[63,64] we further ask an important question: Will the morphological change of HAECs here induced by "non-cytotoxic" dose ZIF-8 NPs affect the integrity and permeability of endothelium? To answer this question, we conducted an endothelial permeability assay by growing a confluent layer of HAECs on a porous transwell insert, exposing the endothelial layer to ZIF-8 NPs, and then quantifying the amount of FITC-dextran that can translocate across the endothelial barrier (Fig. 2A). Here, the amount of FITC-dextran eventually detected in the bottom chamber provides a quantitative measure for the endothelial permeability. The results showed that treating the confluent HAEC layer with ZIF-8 NPs increased endothelial permeability in a dose- and time-dependent fashion (Fig. 2B and S10), a similar trend that can be correlated with the HAEC uptake of ZIF-8 NPs (Fig. 1G-1 J). Specifically, after a period of incubation (24 h) with 25 and 50 μg/mL ZIF-8 NPs, we observed a 1.9-fold and a 2.8-fold increase, respectively, in the FITC-dextran transport across the endothelial barrier (Fig. 2B), suggesting that ZIF-8 nanoparticle treated endothelial barrier became more permeable. In contrast, the lower dose of ZIF-8 NPs (3 μg/mL) caused the negligible increase of FITC-dextran transport (**Figure S11**). To interrogate whether the cellular uptake of ZIF-8 NPs or the extracellular degradation of ZIF-8 NPs (e.g., zinc ions and 2-methylimidazole in cell medium) caused the increased endothelial permeability, we conducted two control experiments: (1) Treating the confluent HAEC layer with ZIF-8 nanoparticle pre-treated cell medium (i.e., incubating ZIF-8 NPs with cell medium for 24 h and then removing the particles through centrifugation to obtain supernatant); and (2) Treating the confluent HAEC layer with cell media containing zinc nitrate and 2-methylimidazole for 24 h, assuming ~ 10 % and ~ 100 % degradation of ZIF-8 NPs in cell media within 24 h. The results of the permeability assay indicated that both ZIF-8 pre-treated cell medium and ~ 10 % degradation of ZIF-8 NPs did not increase the FITC-dextran transport, and ~ 100 % degradation of ZIF-8 NPs (an extreme situation) only caused a slight increase in the FITC-dextran transport (i.e., 1.5-fold). These results suggest that the internalization of ZIF-8 NPs by HAECs, not extracellular nanoparticle degradation, plays a major role in the increased endothelial permeability of the HAEC layer (**Figure S12**). The importance of cellular internalization of particles was further supported by treating endothelial monolayer with larger size of ZIF-8 particles (1019.2 ± 94.3 nm in diameter, 50 μg/mL for 24 h), which corresponded to a lower cellular uptake and negligible impact on the endothelial permeability (**Figure S13**).

It is known that the integrity and permeability of the endothelial barrier are dependent on the intact cell junctions.[65] A confluent endothelial barrier with intact cell junctions restricts the transport of FITC-dextran, whereas the disrupted cell junctions can result in the enlarged gaps between adjacent endothelial cells, facilitating the passage of FITC-dextran. Here, the intact cell junctions are maintained by pairs of transmembrane VE-cadherin through VE-cadherin homophilic interactions.[66–67] Thus, we further inspected HAEC junctions by immunofluorescence staining of the cell junction protein, VE-cadherin. As shown in Fig. 2C and S14, VE-cadherin proteins were found to locate along the cell junctions, profiling the boundary of individual endothelial cells. Clearly, the untreated HAECs possessed integral cell–cell contacts through interacting VE-cadherin, whereas the ZIF-8 nanoparticle treatments caused micrometer-sized gaps between neighboring cells, as marked by red arrowheads (Fig. 2C and S14). Around the gap regions, it was also perceivable that the amount of VE-cadherin significantly decreased, causing a breakdown in cell–cell contacts. The decrease of membrane VE-cadherin was further confirmed by Western blotting (**Figure S15**). By measuring the area of the gaps, we found that the higher doses of ZIF-8 NPs induced larger and more gaps on the otherwise confluent monolayer (Fig. 2D), in accordance with the FITC-dextran transport data (Fig. 2C). These results indicate that "non-cytotoxic" dose ZIF-8 NPs increased the endothelial permeability and gap formation by disrupting the cell junctions of HAECs.

We next asked how are the cell junctions disrupted by "non-cytotoxic" doses of ZIF-8 NPs? Previous studies demonstrated that gold and titanium dioxide nanoparticles induced leakiness of microvascular endothelial barriers by directly binding to VE-cadherin.[67–68] However, it is unlikely that ZIF-8 NPs can directly interact with VE-cadherin in our case since the HAECs here, as macrovascular endothelial cells, have much smaller tight junction size of 1–3 nm located on the apical surface of cell junctions,[69–70] preventing the direct contact of ZIF-8 NPs with VE-cadherin in the underlying adherens junctions. Thus, we switched our focus to the actin cytoskeleton of HAECs, the intracellular structure that physically connects to the transmembrane VE-cadherin and regulates the integrity of cell–cell contacts.[71] Fig. 2E and S16 summarize the fluorescence staining of F-actin of HAEC layers subjected to different treatments. The untreated HAECs (i.e., the control group) showed well-aligned and evenly distributed actin stress fibers across the entire cell body. However, after treatment

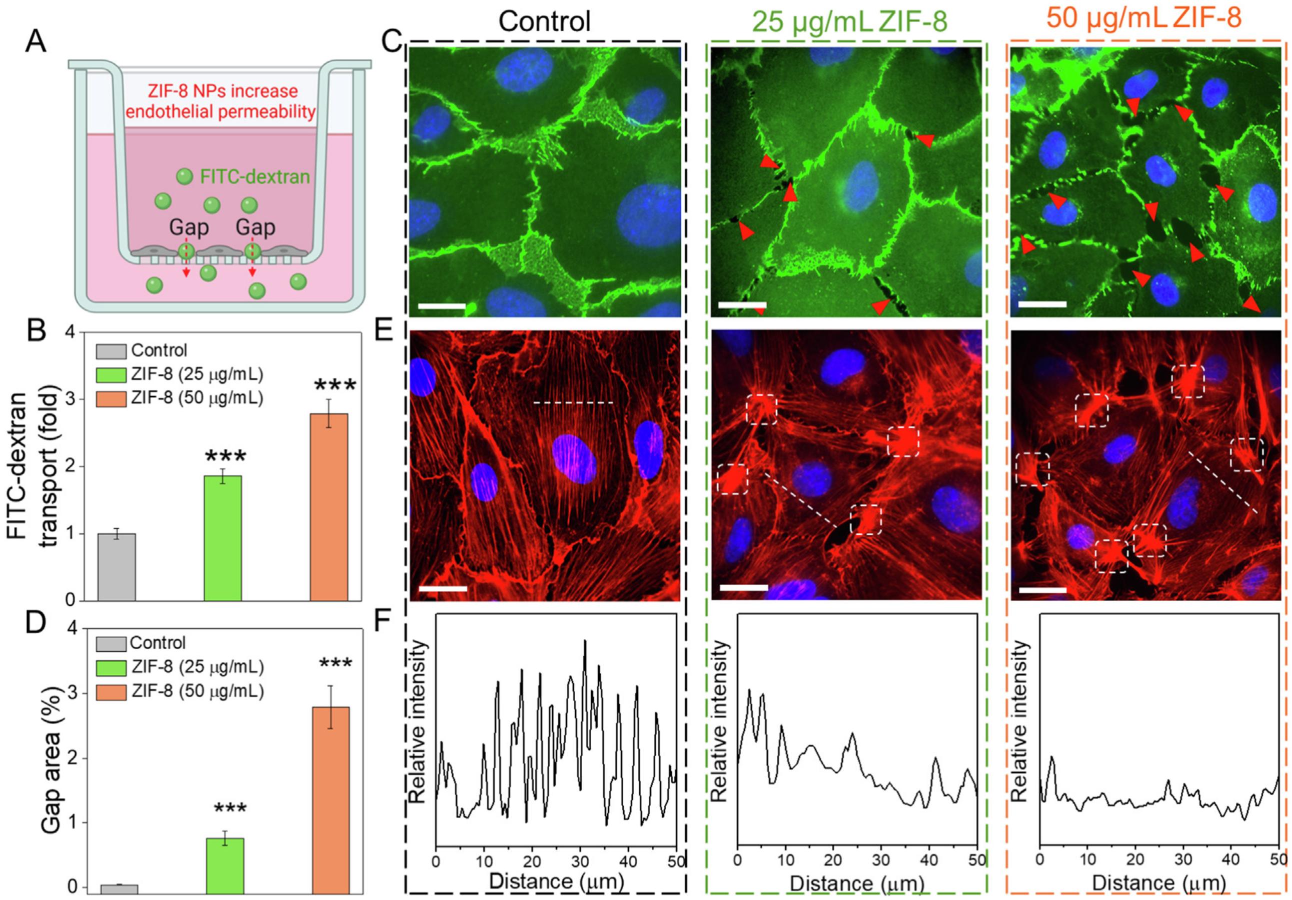

Fig. 2. (A) Schematic illustrating the working principle of endothelial permeability assay. (B) Quantitative analysis of FITC-dextran transport across the HAEC monolayer after different treatments (untreated HAECs as control, HAECs treated by 25 and 50 μg/mL ZIF-8 NPs for 24 h). Data are mean ± SD, n = 5. One-way ANOVA test, ***P < 0.001. (C) Immunofluorescence staining of VE-cadherin showing the formation of intercellular gaps (red arrowheads) on HAEC monolayer after ZIF-8 NPs treatments. Green: VE-cadherin. Blue: nucleus. Scale bars: 30 μm. (D) Quantification analysis of gap area indicating ZIF-8 NPs increased endothelial permeability in a dose-dependent manner. Data are mean ± SD, n = 10. One-way ANOVA test, ***P < 0.001. (E) Fluorescence staining of actin cytoskeleton of HAECs after different treatments. ZIF-8 NPs treatments altered actin organization in HAEC monolayer. (F) The intracellular fluorescence profiles (along dotted lines in E) indicating the reduced actin stress fibers after ZIF-8 NPs treatments. (For interpretation of the references to colour in this figure legend, the reader is referred to the web version of this article.)

with "non-cytotoxic" dose ZIF-8 NPs, the HAECs displayed fewer stress fibers (Fig. 2F), along with more branched actin filaments (marked by white dotted boxes in Fig. 2E). Notably, the branched actin filaments were mostly located around the gap areas, implying the important role of actin structure in the gap formation. Considering the reduced VE-cadherin around the gap areas, it is possible that the branched actin network generated a localized contraction force to pull VE-cadherin toward the intracellular space, disrupting the cell–cell contacts and enlarging the intercellular gaps. Based on these collective data, we propose that the cellular uptake of ZIF-8 NPs, even at "non-cytotoxic" doses, disrupts the cell junctions by causing the reorganization of actin filaments and the change of cell morphology.

2.4. ZIF-8 NPs cause actin reorganization of a single HAEC

To further investigate whether ZIF-8 NPs would change the actin structure and morphology of HAECs, we applied a single-cell imaging tool, atomic force microscopy (AFM), to characterize the single HAEC with or without ZIF-8 nanoparticle treatments. Compared to imaging an HAEC monolayer, examining an HAEC at the single cell level allows for more detailed quantitative characterization of the actin cytoskeleton and cell morphology. Here, Peak-Force quantitative nanomechanical mapping, a unique mode under AFM, was employed to image single, live cells, allowing a simultaneous collection of cell morphology, surface topography, and Young's modulus images of HAECs.[72–74] Importantly, the Young's modulus image provides a clear visualization of actin structures located in the dorsal layer of HAECs as they are the main contributor to cell stiffness (Fig. 3A).[75–77] The Young's modulus value (unit: kPa) for each pixel in the modulus image was calculated by fitting the indentation force curve obtained on that particular coordinate (x,y) using a Hertz model (Fig. 3B). Fig. 3C includes the images of untreated and treated HAECs in three imaging channels. For the untreated HAECs, the cells showed elongated, cobblestone-like morphology, and well-aligned actin stress fibers along the entire cell body including the thick central area and the thin periphery of the cells. Notably, these actin stress fibers were mostly parallel with the long axis of the cell and exhibited precise spatial correlation among the three imaging channels. In stark contrast, HAECs treated by ZIF-8 NPs presented an altered actin organization and cell morphology. For the HAECs treated by 25 μg/mL ZIF-8 NPs, actin filaments parallel with the cell's long axis can only be found in the periphery of cells, while the actin filaments in the central area became disorganized. HAECs treated by 50 μg/mL ZIF-8 NPs showed even more disorganized and branched actin filaments in both central and peripheral regions of the cells, along with rounded cell shape as manifested by the decrease in the aspect ratio of individual cells from 1.75 to 1.22 (**Figure S17**). More AFM images for the untreated and treated HAECs are

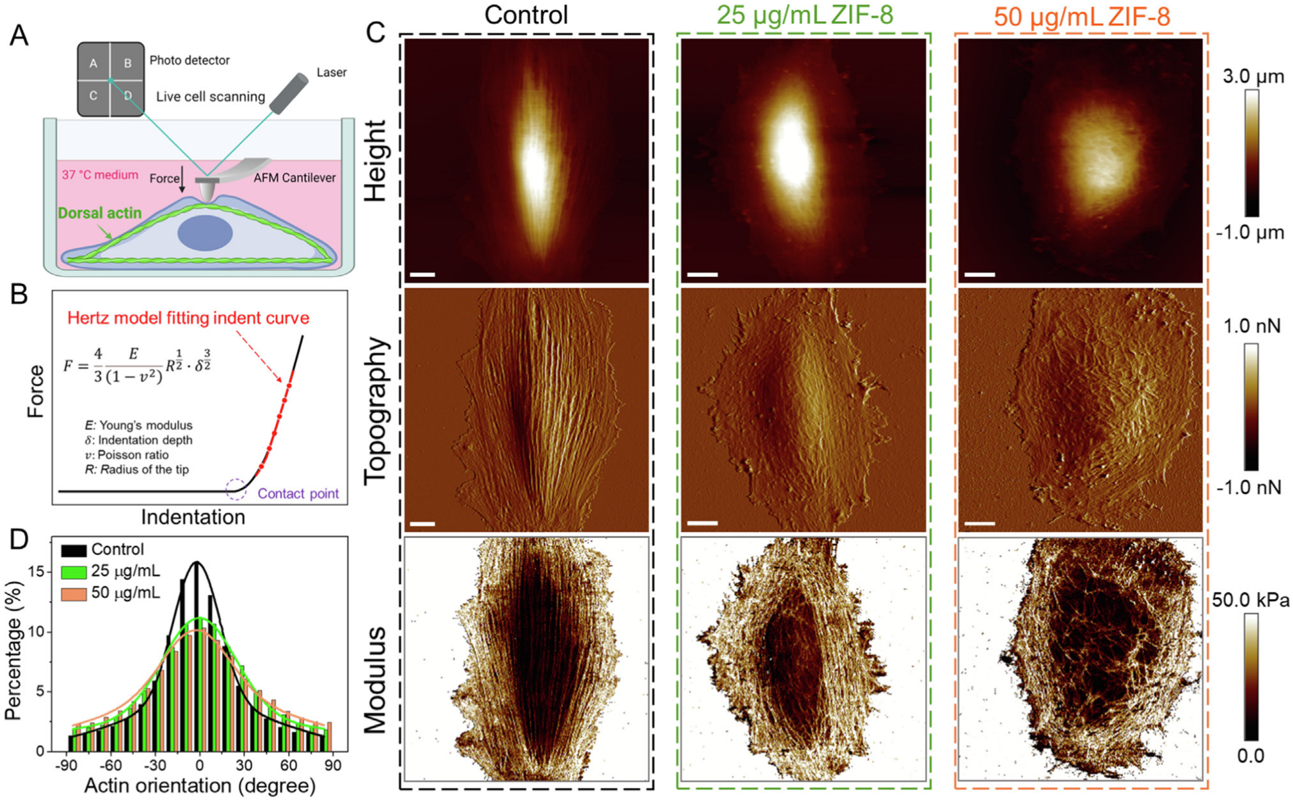

Fig. 3. (A) Schematic illustrating the use of nanomechanical AFM for characterization of dorsal actin underlying the cell membrane of live HAECs. (B) Determination of the Young's modulus for a particular pixel utilizing the Hertz model. (C) Height, surface topography, and Young's modulus images of single HAECs after different treatments (i.e., incubating with 0, 25, and 50 μg/mL ZIF-8 NPs after 24 h). (D) Quantitative analysis of actin orientation in AFM images showing more dispersed actin orientation after ZIF-8 NPs treatments. Scale bars: 10 μm.

presented in **Figure S18-S20**. To quantify the actin change, we analyzed the orientation of actin filaments in AFM images using our custom-made program developed in MATLAB.[78–79] We found that ZIF-8 nanoparticle treatments caused an increased dispersion of actin orientation in HAECs (Fig. 3D). Particularly, the summarized percentage frequency of the actin filaments around the dominant orientation angle (-10 to 10°, −20 to 20°) showed a decreased trend after the treatments, further substantiating the disorganized actin structures induced by ZIF-8 NPs (**Figure S21**).

We further examined the actin structure at the ventral layer of HAECs using direct stochastic optical reconstruction microscopy (dSTORM), a super resolution imaging tool integrated with total internal reflection illumination (TIRF) microscopy. The TIRF microscopy illuminates fluorescence-labelled ventral actin located only 100 nm above the coverslip owing to the thin evanescent field penetration depth (Fig. 4A).[80] Compared to widefield microscopy, dSTORM offers a sub-diffraction limited resolution by stochastically activating individual fluorophores, precisely localizing these fluorophores in each imaging frame, and reconstructing the super resolution image by stacking thousands of imaging frames collected at different time points (Fig. 4B-4C).[81–84] Fig. 4D showcases the drastically improved imaging resolution of dSTORM versus conventional widefield microscopy. Consistent with the AFM results, the untreated HAECs possessed homogeneously distributed actin filaments mostly parallel with the long axis of the cell throughout the entire cell body. However, HAECs treated with ZIF-8 NPs showed fragmented or disappeared actin filaments in the central area of cells. In the periphery of cells, we observed more actin branches and networks in response to the increase of ZIF-8 nanoparticle doses. More dSTORM images and actin orientation analysis for the untreated and treated HAECs are presented in **Figure S22-S25**. In summary, these two imaging techniques reveal that the so-called "safe" doses of ZIF-8 NPs induced actin reorganization and morphological changes in single HAECs. Thus, it is reasonable to conclude that the altered actin organization and cell morphology were responsible for the increased permeability and gap formation of the endothelial barrier.

2.5. Elevated intracellular zinc directly alters actin assembly

To further understand how ZIF-8 NPs changed the actin organization and cell morphology of HAECs, we began to explore the mechanism of altered actin organization by ZIF-8 NPs. By a careful literature search, we noticed that earlier cytotoxicity studies on metal-based nanoparticles generally proposed two actin-disrupting mechanisms: (1) The oxidative stress by internalized metal-based nanoparticles produces reactive oxygen species (ROS), and the increase of ROS in cells can alter actin assembly process because actin and actin-binding proteins are sensitive to ROS levels [85,86]. Chemically inert gold nanoparticles represent a typical example of this mechanism [12,87,88], (2) In the case of degradable nanoparticles, the elevated intracellular metal ions due to the degradation of endocytosed metal-based nanoparticles can either increase the ROS level to indirectly change the actin assembly, or directly participate and alter the actin assembly process [9,89–92]. However, it is worth noting that the majority of previous research was conducted under cytotoxic doses of nanoparticles in which the cell viability or membrane integrity were significantly compromised. It is still unclear how non-cytotoxic doses of metal-based nanoparticles affect the actin organization.

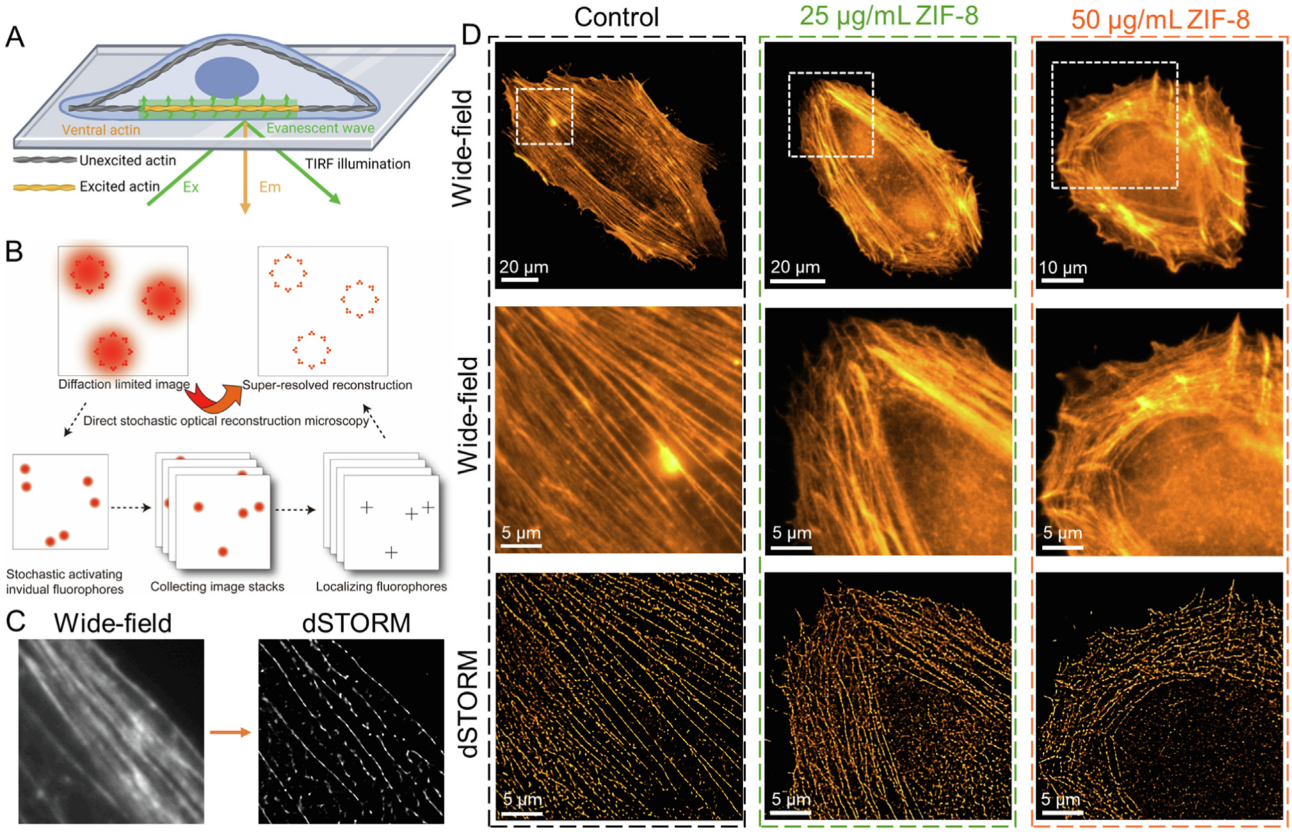

Fig. 4. (A) Diagram depicting the TIRF setup for identifying ventral actin organization in single HAECs. (B-C) The workflow of dSTORM: stochastically activating individual fluorophores, precisely localizing these fluorophores in each imaging frame, and reconstructing the super resolution image by stacking thousands of imaging frames collected at different time points. (D) The ventral actin organization in untreated, 25 μg/mL ZIF-8 treated, and 50 μg/mL ZIF-8 treated HAECs imaged using wide-field and dSTORM microscopy. White dotted boxes mark the zoom-in areas for dSTORM imaging.

Based on these considerations, we first measured the ROS level of HAECs after different treatments, including untreated HAECs (the control group), and HAECs treated with ZIF-8 NPs at concentrations of 25 and 50 μg/mL (**Figure S26**). The ROS assay indicated that the intracellular ROS level of ZIF-8 treated HAECs did not show obvious increase compared to the untreated group, implying that the ROS level may not be the cause of altered actin organization when HAECs were subjected to "non-cytotoxic" doses of ZIF-8 NPs. Indeed, these results are consistent with our earlier cell viability measurements, in which the "non-cytotoxic" doses of ZIF-8 NPs (25 and 50 μg/mL) did not induce the mitochondrial damage (i.e., XTT assay detects mitochondrial function). Then we turned to determine the intracellular zinc ion (Zn^{2+}) concentration in the different HAEC groups. Interestingly, we observed considerable increases in intracellular Zn^{2+} in the ZIF-8 treated HAECs. The HAECs treated with 25 and 50 μg/mL ZIF-8 NPs manifested a 1.7-fold and a 2.9-fold increase in the intracellular Zn^{2+}, respectively, compared to the control group (**Figure S25**). Together, these analyses eliminate the involvement of ROS in the altered actin structures and thus inspired us to form the following hypothesis: The increased intracellular Zn^{2+} could cause actin reorganization by directly interfering with the actin assembly process in HAECs.

To validate this hypothesis, an actin assembly assay was conducted by adjusting the Zn^{2+} concentrations upon the actin polymerization, aiming to mimic what will happen when intracellular Zn^{2+} increases and how this will impact the actin assembly in the cells. Here, the actin assembly assay serves as a simplified model to comprehend the impact of increased intracellular Zn^{2+} on the actin organization of HAECs [93–95]. As shown in AFM images (Fig. 5A and S27), the actin monomer (i.e., globular actin) can assemble to single, linear actin filaments under a normal polymerization condition.[96–97] In stark contrast, when we increased the Zn^{2+} concentrations in the polymerization buffer (resulting in a 2.9-fold increase in the concentration of divalent metal ions, as quantified in HAECs) to mimic the ZIF-8 nanoparticle treated HAECs, we observed branched and thick actin bundles and networks (Fig. 5B and S28). This is in line with previous studies that actin protein contains multiple binding sites for divalent metal ions and the presence of these metal ions can alter the assembly process of actin filaments.[98–100] Intriguingly, the "octopus"-like actin branches are morphologically similar to the actin structures observed from the AFM and dSTORM images of single HAECs, where the actin stress fibers lost their dominant parallel orientation and reorganized to actin branches and networks (Fig. 3 and Fig. 4). These results support our hypothesis that the higher quantities of intracellular Zn^{2+} have the potential to directly affect the actin assembly and change the actin organization in HAECs. We illustrate the proposed actin-disrupting mechanism in HAECs in Fig. 5C: In normal HAECs, the actin monomer can polymerize to form single filamentous actin and subsequently assemble to well-oriented actin bundles (i.e., stress fibers) to maintain the endothelial cell morphology, cell tension, and integrity of cell junctions. However, the elevated intracellular Zn^{2+} caused by the degradation of internalized ZIF-8 NPs in acidic endosome/lysosome alters the actin assembly process,[101–102] leading to changed actin organization, cell morphology, and cell tension, thereby resulting in disrupted cell junctions and increased endothelial permeability.

In addition to endothelial cells, this phenomenon was also observed on another cell model. Considering the increased interest

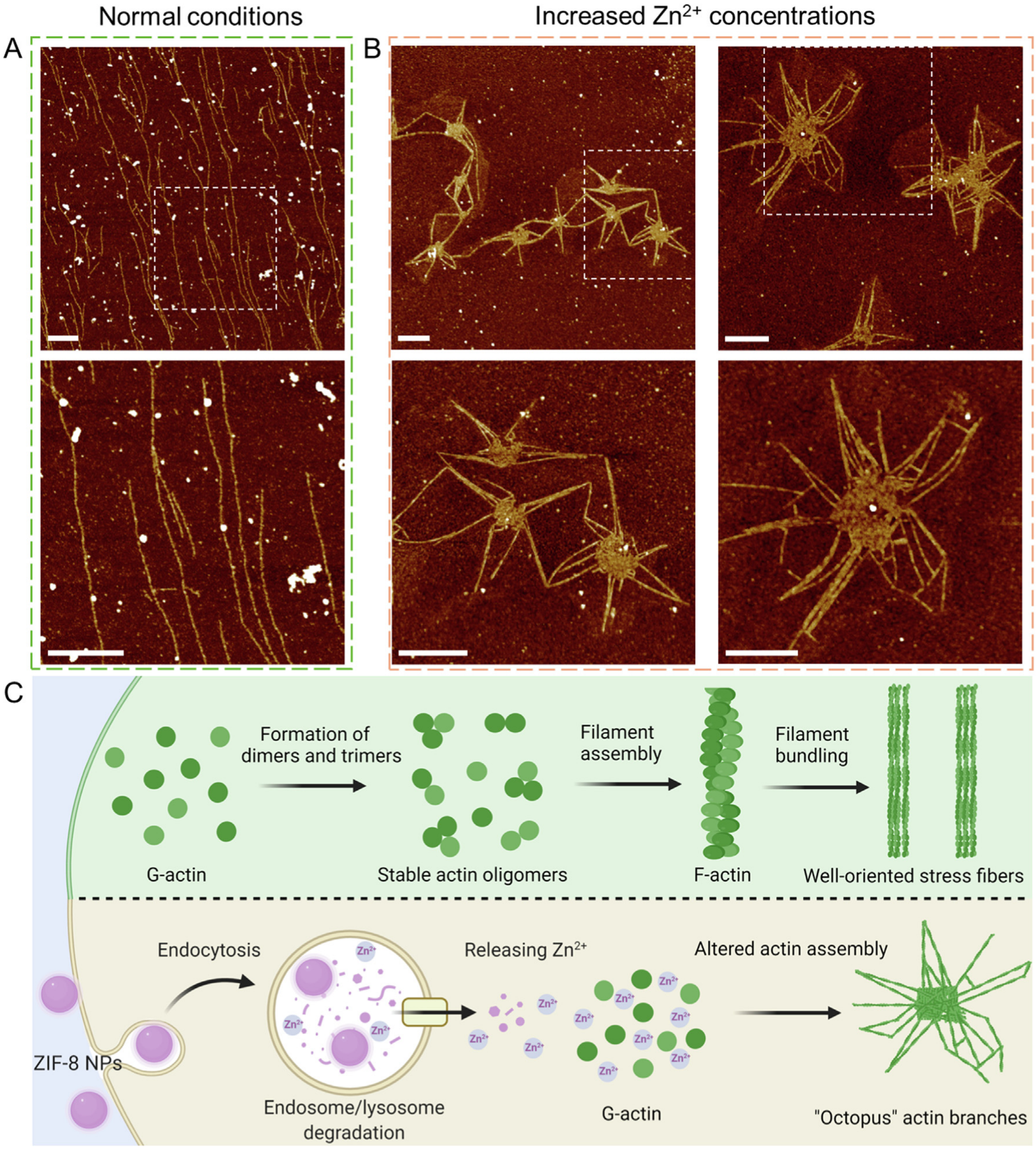

Fig. 5. Actin assembly assay investigating the actin assembly process in the presence of elevated zinc ions. (A) AFM images of typical G-actin-polymerized single, linear actin filaments under normal conditions. Scale bars: 0.5 μm. (B) AFM images of altered actin structures polymerized from G-actin upon elevated Zn^{2+} concentrations. White dotted boxes mark the zoom-in areas. Scale bars: 0.5 μm. (C) Schematic illustrating the mechanism of actin reorganization in HAECs. Without treatment, the G-actin can form stable actin oligomers, further assemble to single, linear actin filaments, and then form actin bundles (i.e., the well-aligned actin stress fibers). After cellular uptake of ZIF-8 NPs, ZIF-8 NPs can be degraded in acidic endosome/lysosome, releasing Zn^{2+} into cytoplasm. The increase of intracellular Zn^{2+} concentration can directly alter the actin assembly process, leading to ''octopus''-like actin structures.

of ZIF-8 based vaccination,[26,103] which is usually administered through subcutaneous injections, we further studied if the ''noncytotoxic'' dose of ZIF-8 NPs can affect the cell morphology and actin cytoskeleton of RAW 264.7 macrophages. Our fluorescence imaging results support a similar conclusion: After treated by a 'noncytotoxic'' dose of ZIF-8 NPs for 24 h (50 μg/mL), the RAW 264.7 macrophages became smaller in size and also showed altered actin cytoskeleton (i.e., more actin aggregates after the treatment, **Figure S29-S30**). Together, these results suggest that actin cytoskeleton and cell morphology could be more sensitive indictors of nanoparticle cytotoxicity for a variety of cell models, and these biophysical changes of cells should not be overlooked. It is also worth noting that microtubules and intermediate filaments are other two cytoskeletal components and it would be interesting to look at how they were affected. However, we mainly focused on actin cytoskeleton because of the major role of actin in the regulation of endothelial junctions and endothelial permeability.

3. Conclusion

We have demonstrated that HAEC uptake of ''non-cytotoxic'' doses of ZIF-8 NPs can increase the endothelial permeability of an HAEC monolayer. The ''non-cytotoxic'' doses were pre-determined by a series of conventional biochemical assays, in which the HAECs maintained over 90 % viability and membrane integrity after exposure to ZIF-8 NPs. Through immunofluorescence staining of VE-cadherin and actin cytoskeleton of ZIF-8 treated HAEC monolayer, we found that the increased endothelial permeability was accompanied with increased gap formation and disrupted cell junctions between adjacent HAECs, as well as reorganized actin structures within HAECs. Nanomechanical AFM and dSTORM further confirmed the alterations in actin cytoskeleton and cell morphology at the single HAEC level, which includes the loss of well-aligned actin stress fibers, the development of actin branches and network, and a decrease in cell aspect ratio. After eliminating the involvement of oxidative stress in the altered actin structures, we hypothesized that the altered actin organization and cell morphology could be attributed to the elevated intracellular Zn^{2+} following endosomal/lysosomal degradation of ZIF-8 NPs. A simplified actin assembly assay validated this hypothesis, suggesting that elevated Zn ions could directly interfere with the actin assembly process and lead to the actin reorganization observed in HAECs. Considering that endothelial permeability plays an indispensable role in a number of physiological and pathological processes, especially the development of cardiovascular diseases and cancer metastasis,[104–106] it is rational to believe that "non-cytotoxic" doses of ZIF-8 NPs, intentionally or unintentionally introduced into blood circulation, may still pose a threat to human health. From a broad view of cytotoxicity evaluation, the biophysical properties of vascular endothelial cells including actin structure and cell morphology can serve as novel and more sensitive markers (compared to biochemical assays) for safety assessment of nanomaterials.

4. Experiments

4.1. Materials

Vascular cell basal medium and endothelial cell growth kit-VEGF were purchased from ATCC. PBS buffer, DPBS buffer, penicillin, and streptomycin were obtained from Gibco. Zinc nitrate hexahydrate ($Zn(NO_3)_2 \cdot 6H_2O$, ≥98 %), 2-methylimidazole (≥99 %), fluorescein isothiocyanate (FITC, ≥90 %), cysteamine (≥98 %), catalase (≥4,000 units/mg protein), glucose oxidase (≥100,000 units/g solid), glucose (≥99.5 %), MES hydrate (≥99.5 %), sodium chloride (≥99 %), magnesium chloride (≥98 %), Tris (hydroxymethyl)aminomethane (≥99.8 %), and Triton X-100 were purchased from Sigma-Aldrich.

4.2. Preparation and characterization of ZIF-8 NPs

The size controlled ZIF-8 NPs and FITC@ZIF-8 NPs with an expected size at around 60 nm were prepared using a previously reported approach.[45] First, a 10 mL of methanol was used to dissolve $Zn(NO_3)_2 \cdot 6H_2O$ (0.2 g) and 2-methylimidazole (0.44 g), respectively. Subsequently, 2-methlimidazole methanol solution was added into the $Zn(NO_3)_2 \cdot 6H_2O$ methanol solution in a dropwise fashion and then the mixed solution was stirred at room temperature for 5 min. Finally, the ZIF-8 NPs were collected and washed three times by methanol using centrifugation (7,000 rpm for 10 min in each time) and stored in methanol for future use. To prepare a larger size ZIF-8 particles, 2 mL of 2-methylimidazole aqueous solution (210.2 mg/mL) were added into 2 mL $Zn(NO_3)_2 \cdot 6H_2O$ aqueous solution (35.12 mg/mL) and the mixture was stirred for 24 h, followed by three times of washing using ultrapure water (4,000 rpm for 10 min in each time). The final product was stored in deionized water.

JEOL JEM 2100 transmission electron microscope and Helios 5 CX scanning electron microscope were utilized to determine the shape and size of synthesized NPs in the dry state. Powder X-ray diffraction (Bruker, D8-Advance) was carried out to investigate the crystallinity of NPs. Dynamic light scattering (Malvern, Zetasizer Nano ZS) was applied to determine the hydrodynamic size of ZIF-8 NPs in different aqueous media.

4.3. SDS-PAGE of protein corona

A series of ZIF-8 NPs (1, 2, and 5 mg/mL) were incubated with HAEC cell medium at 37 °C and 5 % CO_2 incubator for 24 h. Next, the pellets of ZIF-8 NPs were collected and washed by three times of centrifugation (7,000 rpm for 10 min in each time). To elute the adsorbed proteins on the ZIF-8 NPs, the pellets were resuspended in SDS-sample buffer (Bio-Rad, 1610747) and boiled for 5 mins at 90 °C. The SDS-PAGE with all samples was performed using a 4–20 % precast polyacrylamide gel. 0.5 mg/mL BSA and 1 % FBS were used as the control samples.

4.4. Cytotoxicity of ZIF-8 NPs on HAEC cells

Normal Primary Human Aortic Endothelial Cells (HAECs) were purchased from ATCC (PCS-100–011). The HAECs were grown in vascular cell basal medium supplemented with the endothelial cell growth kit-VEGF and incubated at 37 °C and 5 % CO_2 incubator according to manufacturer's instruction. Three commonly used cytotoxicity assays, XTT, LDH, and live/dead staining assays were applied to evaluate the cytotoxic effect of ZIF-8 NPs on HAECs. For XTT and LDH assays, in a 96-well plate, the HAECs were seeded at a density of 5,000 cells/cm^2. After 12 h cell culture, each well was filled with growth medium containing varied concentrations of ZIF-8 NPs (0, 3, 6, 12, 25, 50, 75, and 100 μg/mL) and cultured with cells for 24 h. Thereafter, the free (un-internalized) ZIF-8 NPs in the supernatant were replaced by XTT (X12223), LDH (C20301), or live/dead staining (R37609) reagents purchased from Thermo Fisher Scientific to measure the cell viability or membrane integrity.

4.5. HAEC uptake of ZIF-8 NPs

The internalization of ZIF-8 NPs by HAECs was investigated based on the quantification of correlated total cell fluorescence (CTCF) using fluorescence-labelled FITC@ZIF-8 NPs. The FITC@ZIF-8 were prepared by mixing $Zn(NO_3)_2 \cdot 6H_2O$ and 2-methylimidazole in the presence of FITC in methanol. In detail, 30 μL of 5 mM FITC was added into $Zn(NO_3)_2 \cdot 6H_2O$ methanol solution (20 mg/mL) and then the 2-methylimidazole solution (44 mg/mL in methanol) was added to the mixed solution. After vigorous stirring for 5 min, the synthesized FITC@ZIF-8 NPs were collected by centrifugation (7000 rpm for 10 min), and then washed three times with methanol. To prepare the FITC labelled larger size of ZIF-8 particles, 5 mM FITC was introduced to the above larger ZIF-8 particles synthesis protocol. The HAECs were first cultured on a glass coverslip for overnight. Next, the cells were incubated with FITC@ZIF-8 NPs (0, 25, and 50 μg/mL) for 24 h. A control experiment was conducted by incubating HAECs with free FITC (FITC dissolved in cell medium) for 24 h. For the inhibitor experiment, HAECs were first cultured on a glass coverslip for overnight. Next, the cells were washed, and fresh media supplemented with methyl-β-cyclodextrin (5 mM) was added, followed by a 30 min incubation at 37 °C. After 30 min incubation, the medium was replaced by fresh media containing FITC@ZIF-8 NPs (50 μg/mL), and cells were incubated with nanoparticles for 24 h. After nanoparticle incubation, the cells were gently rinsed with DPBS and fixed with 4 % PFA (Thermo Fisher Scientific, 047392–9 M) for 10 min. During the 24 h incubation period, the internalization of FITC@ZIF-8 NPs were tracked by imaging the cells at time intervals of 6, 12, and 24 h. An Olympus IX71 microscope and EMCCD camera (Andor Ultra iXon 888) were applied to collect fluorescence images on 10 individual cells under each condition. The quantification of the internalized FITC@ZIF-8 NPs within the cells using CTCF was through Image-J software.

4.6. Endothelial permeability assay

A monolayer of HAECs were cultured on a transwell insert (0.4 μm pore, Corning) to reach 100 % confluence (~13,000 cells per well), and then the confluent HAEC monolayer was exposed to cell growth media containing 0, 25, and 50 μg/mL ZIF-8 NPs for 6, 12, and 24 h. After the ZIF-8 nanoparticle treatment, the cell growth medium was removed and 1 mg/mL of FITC-dextran (40 kDa, Sigma-Aldrich, 60842–46-8) solution was added into the transwell. After waiting for 30 min, a fluorescent microplate reader with an excitation/emission wavelength of 490/520 nm was used to measure the amount of FITC-dextran that translocated through the HAEC barrier to the bottom chamber of the well. The FITC-dextran transport across the ZIF-8 nanoparticle treated HAEC layer was normalized to its transport on the untreated HAEC layer (the control group). Two control experiments were conducted: (1) Cell growth medium was incubated with 50 μg/mL ZIF-8 NPs for 24 h. Then the cell medium was collected by removing the ZIF-8 NPs using centrifuge. The obtained cell medium (i.e., ZIF-8 nanoparticle conditioned medium) was used to treat the monolayer of HAECs for 24 h. (2) A monolayer of HAECs was treated with cell medium containing 1.4 μg/mL zinc nitrate and 3.6 μg/mL 2-methylimidazole for 24 h, assuming a 10 % degradation of ZIF-8 NPs in cell medium, or cell medium containing 14 μg/mL zinc nitrate and 36 μg/mL 2-methylimidazole for 24 h, assuming a 100 % degradation of ZIF-8 NPs within 24 h. After these two types of treatments, the HAEC permeability assays were conducted.

4.7. Fluorescence staining of VE-cadherin and actin cytoskeleton

The fluorescence staining of VE-cadherin and actin filaments allowed for the visualization of cell junctions and actin cytoskeleton, respectively. In a 50 mm glass-bottom dish, HAECs were plated at a density of 5,000 cells/cm^2 and cultivated until they formed a confluent monolayer. The monolayer of HAECs was next subjected to a 24 h treatment with cell growth medium containing ZIF-8 NPs at concentrations of 0, 25, and 50 μg/mL. After ZIF-8 nanoparticle treatment, the cells were rinsed with DPBS, fixed with 4 % PFA for 10 min, permeabilized with 0.1 % Triton-X 100 for 10 min, blocked with BlockAid blocking solution (Thermo Fisher Scientific, B10710), and incubated with 1:200 dilution of VE-cadherin primary antibody (Cell Signaling Technology, 2500S) for overnight at 4 °C, followed by 1 h incubation with 1:400 dilution of secondary antibody (Cell Signaling Technology, 4412S). RAW 264.7 macrophage was cultured in DMEM medium with 10 % FBS in a 37 °C and 5 % CO_2 incubator. 20,000 RAW 264.7 cells were cultured on a coverslip (25 mm diameter) for 24 h. Next, the cells were incubated with ZIF-8 NPs (0 and 50 μg/mL) for another 24 h. After ZIF-8 NPs treatment, the cells were fixed with 4 % PFA, followed by the fluorescence staining. The actin staining protocol for both HAEC and RAW 264.7 cells with ActinRed 555 ReadyProbes (Thermo Fisher Sciencific, R37112) was following the manufacturer's instruction.

4.8. Western blot analysis of VE-cadherin

The membrane VE-cadherin was extracted by Membrane Protein Extraction Kit (Thermo Fisher, 89842). The protein concentration was quantified by a BCA assay (Thermo Fisher, 23225). The same amount of protein was loaded into a 4–20 % precast SDS-PAGE gel. After running the gel for 90 min under 100 mV, it was transferred to a nitrocellulose membrane (0.2 μm) followed by blocking with EveryBlot blocking buffer (Bio-Rad, 12010020). Then the membrane was incubated with VE-cadherin antibody (Cell Signaling Technology, 2500) and Na K ATPase antibody (Cell Signaling Technology, 3010) for overnight at 4 °C. A goat anti-rabbit IgG antibody with HRP conjugation was used as the secondary antibody. ChemiDoc from Bio-Rad was used for imaging.

4.9. AFM imaging of single, live HAEC

A Peak-Force quantitative nanomechanical imaging mode using BioScope Resolve AFM (Bruker) was applied to investigate the morphology and actin cytoskeleton of individual HAEC. For the ZIF-8 nanoparticle treated cells, 30,000 cells were seeded in a 50 mm glass-bottom imaging dish for overnight and then incubated with 25 or 50 μg/mL ZIF-8 NPs for 24 h. Prior to AFM imaging, the cell medium containing ZIF-8 NPs was replaced by fresh growth medium. Then the single cell imaging was conducted on a temperature-controlled stage (37 °C) using the following imaging parameters: oscillation amplitude (400–600 nm), peak force set point (400–600 pN), peak force frequency (0.25 kHz), and imaging resolution (256 × 256). Post image process and data analysis were conducted by NanoScope Analysis (v1.9, Bruker). The individual force-indentation curves were fitted using the Hertz model to obtain Young's modulus on a single spot based on the spherical geometry of the AFM tip (Bruker, PFQNM-LC-A, tip radius: 70 nm):

$$F = \frac{4}{3}\frac{E}{(1-\nu^2)}R^{\frac{1}{2}}\cdot\delta^{\frac{3}{2}}$$

E: Young's modulus. ν: Poisson ratio (0.5). R: Tip curvature radius. δ: Indentation depth.

AFM surface topography images were used to detect the orientation of submembranous actin stress fibers as described previously described. [78] In short, vertical and horizontal spatial gradients were calculated from topography images and subsequently utilized to determine the gradient magnitude and intensity gradient. An algorithm published by Karlon et al. [107] was then used to calculate stress fiber orientation from the gradient magnitude and intensity gradients.

4.10. dSTORM imaging of ventral actin cytoskeleton

The sample preparation for dSTORM imaging was similar to AFM sample preparation. HAECs were grown overnight on a 50 mm imaging dish at initial seeding density of 30,000 cells/dish. Then the cell growth medium was replaced with fresh medium containing 25 or 50 μg/mL ZIF-8 NPs and HAECs were treated for 24 h. After treatment with ZIF-8 NPs, the HAECs were fixed to preserve actin structure using 4 % PFA in PBS buffer and then permeabilized with 0.1 % Triton X-100 in an actin-stabilizing buffer containing 10 mM MES pH 6.1, 150 mM NaCl, 5 mM EGTA, 5 mM glucose, and 5 mM $MgCl_2$ for 10 min. Then the cell sample was treated with 0.1 % $NaBH_4$ to eliminate the background autofluorescence. The sample was then blocked for 1 h at room temperature with 1 % BSA and stained with 66 μM Alexa Fluor 568 phalloidin dye (Thermo Fisher Scientific, A12380) for overnight at 4 °C. The photo-switching of Alexa Fluor 568 was performed in an imaging buffer (100 mM MEA, 500 μg/mL glucose oxidase, 0.04 mg/mL catalase in Tris-NaCl buffer with 10 % glucose, pH 8). The detailed dSTORM imaging protocol and instrument parameters can be found in our earlier publication.[61] A sequence of 20,000–30,000 frames were recorded for image reconstruction using ThunderSTORM in ImageJ.

The reconstructed dSTORM images were then processed in MATLAB (R2016a, MathWorks Inc. Natick, MA, USA) to measure the orientation of the total cytoskeletal fibers using a series of elongated Laplacian-of-Gaussian (eLoG) filters as described previously.[78] The actin orientation was determined as the rotating eLoG filter that resulted in the highest maximum pixel intensity.

4.11. Intracellular ROS level and zinc concentration

Cellular ROS assay kit (Abcam, ab113851) was used to measure the ROS level in HAECs. This assay uses a cell permeant fluorescent dye, 2′,7′-dichlorodihydrofluorescein diacetate (H2DCFDA), to detect ROS levels in live cells. Intracellular zinc concentration was evaluated by the Zinquin ethyl ester fluorescent indicator (Sigma, Z2251), a cell-permeable fluorescent probe for Zn^{2+}. The HAEC cells were seeded in a 96-well plate at a density of 5,000 cells/well and waited for 24 h. Then, the HAECs were treated with growth medium containing ZIF-8 NPs (25 and 50 μg/mL) for another 24 h. Finally, the ZIF-8 nanoparticle treated cells were washed and then the ROS or Zinc probe were added into the cells. The ROS and zinc levels were measured using a fluorescence microplate reader with the excitation and emission wavelengths set to 485/538 nm and 355/460 nm, respectively.

4.12. Actin assembly assay

G-actin purified from rabbit skeletal muscle (Cytoskeleton, Inc. AKL95) was reconstituted with general actin buffer (Cytoskeleton, Inc. BSA01) containing 0.2 mM ATP (Cytoskeleton, Inc. BSA04) and 0.5 mM DTT (Thermo Fisher Scientific, D1532) on ice for 1 h. After 15 min centrifugation (14,000 rpm) at 4 °C, the supernatant was transferred to a fresh tube. Next, the polymerization of G-actin to F-actin was induced by the addition of 1/10 vol of 10 × polymerization buffer (Cytoskeleton, Inc. BSA02) to the above G-actin solution. The polymerization was allowed at room temperature for 1 h (the control group). For the Zn^{2+} treated group, a 2.9-fold increase in the concentration of divalent metal ions was achieved by adding zinc nitrate hexahydrate to the polymerization process. Amicon ultra centrifugal filters (Sigma, cutoff: 100 kDa) were used to purify the assembled actin filaments under centrifugation at 7000 rpm for 10 min. Then the purified actin filaments were adsorbed on mica for AFM imaging. SCANASYST-AIR mode was applied to image the actin filaments from control and Zn^{2+} treated samples.

CRediT authorship contribution statement

Jinyuan Liu: Methodology, Formal analysis, Investigation, Validation, Writing – original draft, Visualization. **Alex Rickel:** Methodology, Formal analysis. **Steve Smith:** Funding acquisition, Writing – review & editing. **Zhongkui Hong:** Conceptualization, Software, Funding acquisition, Supervision, Writing – review & editing. **Congzhou Wang:** Conceptualization, Validation, Funding acquisition, Supervision, Writing – review & editing, Project administration.

Data availability

Data will be made available on request.

Declaration of Competing Interest

The authors declare that they have no known competing financial interests or personal relationships that could have appeared to influence the work reported in this paper.

Acknowledgements

The authors thank the support from the National Science Foundation CAREER Award (Award number: 2143972), the National Institutes of Health through the Award R03EB028869 (PI: Wang) and the Award R15HL147214 (PI: Hong), and the State of South Dakota Board of Regents through the IMAGEN Biomaterials Collaborative Grant.

Appendix A. Supplementary material

Supplementary data to this article can be found online at https://doi.org/10.1016/j.jcis.2022.12.020.

References

[1] R. Ettlinger, U. Lächelt, R. Gref, P. Horcajada, T. Lammers, C. Serre, P. Couvreur, R.E. Morris, S. Wuttke, Toxicity of metal–organic framework nanoparticles: from essential analyses to potential applications, Chem. Soc. Rev. 51 (2) (2022) 464–484.
[2] A. Kroll, M.H. Pillukat, D. Hahn, J. Schnekenburger, Current in vitro methods in nanoparticle risk assessment: Limitations and challenges, Eur. J. Pharm. Biopharm. 72 (2) (2009) 370–377.
[3] N. Lewinski, V. Colvin, R. Drezek, Cytotoxicity of Nanoparticles, Small 4 (1) (2008) 26–49.
[4] B. Kong, J.H. Seog, L.M. Graham, S.B. Lee, Experimental considerations on the cytotoxicity of nanoparticles, Nanomedicine 6 (5) (2011) 929–941.
[5] A.M. Alkilany, C.J. Murphy, Toxicity and cellular uptake of gold nanoparticles: what we have learned so far?, Journal of nanoparticle research : an interdisciplinary forum for nanoscale science and technology 12 (7) (2010) 2313–2333
[6] Y.-L. Wu, N. Putcha, K.W. Ng, D.T. Leong, C.T. Lim, S.C.J. Loo, X. Chen, Biophysical Responses upon the Interaction of Nanomaterials with Cellular Interfaces, Acc. Chem. Res. 46 (3) (2013) 782–791.
[7] M.A.I. Rasel, S. Singh, T.D. Nguyen, I.O. Afara, Y. Gu, Impact of Nanoparticle Uptake on the Biophysical Properties of Cell for Biomedical Engineering Applications, Sci. Rep. 9 (1) (2019) 5859.
[8] D. Septiadi, F. Crippa, T.L. Moore, B. Rothen-Rutishauser, A. Petri-Fink, Nanoparticle-Cell Interaction: A Cell Mechanics Perspective, Adv. Mater. 30 (19) (2018) 1704463.
[9] L. García-Hevia, R. Valiente, R. Martín-Rodríguez, C. Renero-Lecuna, J. González, L. Rodríguez-Fernández, F. Aguado, J.C. Villegas, M.L. Fanarraga, Nano-ZnO leads to tubulin macrotube assembly and actin bundling, triggering cytoskeletal catastrophe and cell necrosis, Nanoscale 8 (21) (2016) 10963–10973.
[10] C. Gao, Y. Jin, G. Jia, X. Suo, H. Liu, D. Liu, X. Yang, K. Ge, X.-J. Liang, S. Wang, J. Zhang, Y2O3 Nanoparticles Caused Bone Tissue Damage by Breaking the Intracellular Phosphate Balance in Bone Marrow Stromal Cells, ACS Nano 13 (1) (2019) 313–323.
[11] F. Xu, C. Piett, S. Farkas, M. Qazzaz, N.I. Syed, Silver nanoparticles (AgNPs) cause degeneration of cytoskeleton and disrupt synaptic machinery of cultured cortical neurons, Mol. Brain 6 (1) (2013) 29.
[12] X. Ma, R. Hartmann, D. Jimenez de Aberasturi, F. Yang, S.J.H. Soenen, B.B. Manshian, J. Franz, D. Valdeperez, B. Pelaz, N. Feliu, N. Hampp, C. Riethmüller, H. Vieker, N. Frese, A. Gölzhäuser, M. Simonich, R.L. Tanguay, X.-J. Liang, W.J. Parak, Colloidal Gold Nanoparticles Induce Changes in Cellular and Subcellular Morphology, ACS Nano 11 (8) (2017) 7807–7820.
[13] M.I. Setyawati, C. Sevencan, B.H. Bay, J. Xie, Y. Zhang, P. Demokritou, D.T. Leong, Nano-TiO2 Drives Epithelial-Mesenchymal Transition in Intestinal Epithelial Cancer Cells, Small 14 (30) (2018) 1800922.
[14] C. Wang, S. Tadepalli, J. Luan, K.-K. Liu, J.J. Morrissey, E.D. Kharasch, R.R. Naik, S. Singamaneni, Metal-Organic Framework as a Protective Coating for Biodiagnostic Chips, Adv. Mater. 29 (7) (2017) 1604433.
[15] H.-S. Wang, Metal–organic frameworks for biosensing and bioimaging applications, Coord. Chem. Rev. 349 (2017) 139–155.
[16] Y. Zhao, H. Zeng, X.-W. Zhu, W. Lu, D. Li, Metal–organic frameworks as photoluminescent biosensing platforms: mechanisms and applications, Chem. Soc. Rev. 50 (7) (2021) 4484–4513.
[17] Y. Li, H. Guo, Z. Yin, K. Lyle, L. Tian, Metal-Organic Frameworks for Preserving the Functionality of Plasmonic Nanosensors, ACS Appl. Mater. Interfaces 13 (4) (2021) 5564–5573.
[18] J. Andreo, R. Ettlinger, O. Zaremba, Q. Peña, U. Lächelt, R.F. de Luis, R. Freund, S. Canossa, E. Ploetz, W. Zhu, C.S. Diercks, H. Gröger, S. Wuttke, Reticular Nanoscience: Bottom-Up Assembly Nanotechnology, J. Am. Chem. Soc. 144 (17) (2022) 7531–7550.
[19] K. Lu, T. Aung, N. Guo, R. Weichselbaum, W. Lin, Nanoscale Metal-Organic Frameworks for Therapeutic, Imaging, and Sensing Applications, Adv. Mater. 30 (37) (2018) 1707634.
[20] Y. Liu, T. Jiang, Z. Liu, Metal-Organic Frameworks for Bioimaging: Strategies and Challenges, Nanotheranostics 6 (2) (2022) 143–160.

[21] J. Della Rocca, D. Liu, W. Lin, Nanoscale Metal-Organic Frameworks for Biomedical Imaging and Drug Delivery, Acc. Chem. Res. 44 (10) (2011) 957–968.

[22] M. Peller, A. Lanza, S. Wuttke, MRI-Active Metal-Organic Frameworks: Concepts for the Translation from Lab to Clinic, Advanced Therapeutics 4 (9) (2021) 2100067.

[23] K. Böll, P. Hirschle, K. Klingl, A. Zimpel, C. Hirschle, M. Ingrisch, O. Dietrich, S. Wuttke, M. Peller, Tuning the Synergistic Interplay between Clinical MRI Contrast Agents and MR-Active Metal-Organic Framework Nanoparticles, Chem. Mater. 34 (8) (2022) 3862–3871.

[24] K. Liang, R. Ricco, C.M. Doherty, M.J. Styles, S. Bell, N. Kirby, S. Mudie, D. Haylock, A.J. Hill, C.J. Doonan, P. Falcaro, Biomimetic mineralization of metal-organic frameworks as protective coatings for biomacromolecules, Nat. Commun. 6 (1) (2015) 7240.

[25] C. Wang, H. Sun, J. Luan, Q. Jiang, S. Tadepalli, J.J. Morrissey, E.D. Kharasch, S. Singamaneni, Metal-Organic Framework Encapsulation for Biospecimen Preservation, Chem. Mater. 30 (4) (2018) 1291–1300.

[26] M.A. Luzuriaga, R.P. Welch, M. Dharmarwardana, C.E. Benjamin, S. Li, A. Shahrivarkevishahi, S. Popal, L.H. Tuong, C.T. Creswell, J.J. Gassensmith, Enhanced Stability and Controlled Delivery of MOF-Encapsulated Vaccines and Their Immunogenic Response In Vivo, ACS Appl. Mater. Interfaces 11 (10) (2019) 9740–9746.

[27] H. Sun, Y. Li, S. Yu, J. Liu, Metal-organic frameworks (MOFs) for biopreservation: From biomacromolecules, living organisms to biological devices, Nano Today 35 (2020) 100985.

[28] Y. Wang, J. Yan, N. Wen, H. Xiong, S. Cai, Q. He, Y. Hu, D. Peng, Z. Liu, Y. Liu, Metal-organic frameworks for stimuli-responsive drug delivery, Biomaterials 230 (2020) 119619.

[29] M.-X. Wu, Y.-W. Yang, Metal-Organic Framework (MOF)-Based Drug/Cargo Delivery and Cancer Therapy, Adv. Mater. 29 (23) (2017) 1606134.

[30] Y. Liu, Y. Zhao, X. Chen, Bioengineering of Metal-organic Frameworks for Nanomedicine, Theranostics 9 (11) (2019) 3122–3133.

[31] E. Ploetz, H. Engelke, U. Lächelt, S. Wuttke, The Chemistry of Reticular Framework Nanoparticles: MOF, ZIF, and COF Materials, Adv. Funct. Mater. 30 (41) (2020) 1909062.

[32] A. Carné-Sánchez, J. Albalad, T. Grancha, I. Imaz, J. Juanhuix, P. Larpent, S. Furukawa, D. Maspoch, Postsynthetic Covalent and Coordination Functionalization of Rhodium(II)-Based Metal-Organic Polyhedra, J. Am. Chem. Soc. 141 (9) (2019) 4094–4102.

[33] M. Lismont, L. Dreesen, S. Wuttke, Metal-Organic Framework Nanoparticles in Photodynamic Therapy: Current Status and Perspectives, Adv. Funct. Mater. 27 (14) (2017) 1606314.

[34] R. Freund, U. Lächelt, T. Gruber, B. Rühle, S. Wuttke, Multifunctional Efficiency: Extending the Concept of Atom Economy to Functional Nanomaterials, ACS Nano 12 (3) (2018) 2094–2105.

[35] E. Ploetz, A. Zimpel, V. Cauda, D. Bauer, D.C. Lamb, C. Haisch, S. Zahler, A.M. Vollmar, S. Wuttke, H. Engelke, Metal-Organic Framework Nanoparticles Induce Pyroptosis in Cells Controlled by the Extracellular pH, Adv. Mater. 32 (19) (2020) 1907267.

[36] H. Zheng, Y. Zhang, L. Liu, W. Wan, P. Guo, A.M. Nyström, X. Zou, One-pot Synthesis of Metal-Organic Frameworks with Encapsulated Target Molecules and Their Applications for Controlled Drug Delivery, J. Am. Chem. Soc. 138 (3) (2016) 962–968.

[37] T.-T. Chen, J.-T. Yi, Y.-Y. Zhao, X. Chu, Biomineralized Metal-Organic Framework Nanoparticles Enable Intracellular Delivery and Endo-Lysosomal Release of Native Active Proteins, J. Am. Chem. Soc. 140 (31) (2018) 9912–9920.

[38] Y. Li, K. Zhang, P. Liu, M. Chen, Y. Zhong, Q. Ye, M.Q. Wei, H. Zhao, Z. Tang, Encapsulation of Plasmid DNA by Nanoscale Metal-Organic Frameworks for Efficient Gene Transportation and Expression, Adv. Mater. 31 (29) (2019) 1901570.

[39] W.-H. Chen, G.-F. Luo, M. Vázquez-González, R. Cazelles, Y.S. Sohn, R. Nechushtai, Y. Mandel, I. Willner, Glucose-Responsive Metal–Organic-Framework Nanoparticles Act as "Smart" Sense-and-Treat Carriers, ACS Nano 12 (8) (2018) 7538–7545.

[40] C. Wang, G. Sudlow, Z. Wang, S. Cao, Q. Jiang, A. Neiner, J.J. Morrissey, E.D. Kharasch, S. Achilefu, S. Singamaneni, Metal-Organic Framework Encapsulation Preserves the Bioactivity of Protein Therapeutics, Adv. Healthc. Mater. 7 (22) (2018) 1800950.

[41] S.K. Alsaiari, S. Patil, M. Alyami, K.O. Alamoudi, F.A. Aleisa, J.S. Merzaban, M. Li, N.M. Khashab, Endosomal Escape and Delivery of CRISPR/Cas9 Genome Editing Machinery Enabled by Nanoscale Zeolitic Imidazolate Framework, J. Am. Chem. Soc. 140 (1) (2018) 143–146.

[42] Q. Wu, M. Niu, X. Chen, L. Tan, C. Fu, X. Ren, J. Ren, L. Li, K. Xu, H. Zhong, X. Meng, Biocompatible and biodegradable zeolitic imidazolate framework/polydopamine nanocarriers for dual stimulus triggered tumor thermo-chemotherapy, Biomaterials 162 (2018) 132–143.

[43] M. Hoop, C.F. Walde, R. Riccò, F. Mushtaq, A. Terzopoulou, X.-Z. Chen, A.J. deMello, C.J. Doonan, P. Falcaro, B.J. Nelson, J. Puigmartí-Luis, S. Pané, Biocompatibility characteristics of the metal organic framework ZIF-8 for therapeutical applications, Appl. Mater. Today 11 (2018) 13–21.

[44] C. Tamames-Tabar, D. Cunha, E. Imbuluzqueta, F. Ragon, C. Serre, M.J. Blanco-Prieto, P. Horcajada, Cytotoxicity of nanoscaled metal–organic frameworks, J. Mater. Chem. B 2 (3) (2014) 262–271.

[45] J. Zhuang, C.-H. Kuo, L.-Y. Chou, D.-Y. Liu, E. Weerapana, C.-K. Tsung, Optimized Metal–Organic-Framework Nanospheres for Drug Delivery: Evaluation of Small-Molecule Encapsulation, ACS Nano 8 (3) (2014) 2812–2819.

[46] F. Hao, X.-P. Yan, Nano-sized zeolite-like metal-organic frameworks induced hematological effects on red blood cell, J. Hazard. Mater. 424 (2022) 127353.

[47] L. He, G. Huang, H. Liu, C. Sang, X. Liu, T. Chen, Highly bioactive zeolitic imidazolate framework-8–capped nanotherapeutics for efficient reversal of reperfusion-induced injury in ischemic stroke. Science, Advances 6 (12) (2020) eaay9751.

[48] L. Zhang, Z. Wang, Y. Zhang, F. Cao, K. Dong, J. Ren, X. Qu, Erythrocyte Membrane Cloaked Metal-Organic Framework Nanoparticle as Biomimetic Nanoreactor for Starvation-Activated Colon Cancer Therapy, ACS Nano 12 (10) (2018) 10201–10211.

[49] T. Simon-Yarza, A. Mielcarek, P. Couvreur, Nanoparticles of Metal-Organic Frameworks: On the Road to In Vivo Efficacy in Biomedicine. 30 (37) (2018) e1707365.

[50] Y. Wu, T. Yu, T.A. Gilbertson, A. Zhou, H. Xu, K.T. Nguyen, Biophysical Assessment of Single Cell Cytotoxicity: Diesel Exhaust Particle-Treated Human Aortic Endothelial Cells, PLoS One 7 (5) (2012) e36885.

[51] V.G. Walker, Z. Li, T. Hulderman, D. Schwegler-Berry, M.L. Kashon, P.P. Simeonova, Potential in vitro effects of carbon nanotubes on human aortic endothelial cells, Toxicol. Appl. Pharmacol. 236 (3) (2009) 319–328.

[52] N. Miyazawa, M. Abe, T. Souma, M. Tanemoto, T. Abe, M. Nakayama, S. Ito, Methylglyoxal augments intracellular oxidative stress in human aortic endothelial cells, Free Radic. Res. 44 (1) (2010) 101–107.

[53] H.-J. Sun, Z.-Y. Wu, X.-W. Nie, J.-S. Bian, Role of Endothelial Dysfunction in Cardiovascular Diseases: The Link Between Inflammation and Hydrogen Sulfide, Front. Pharmacol. 10 (2020).

[54] C. Michiels, Endothelial cell functions, J. Cell. Physiol. 196 (3) (2003) 430–443.

[55] L. Claesson-Welsh, E. Dejana, D.M. McDonald, Permeability of the Endothelial Barrier: Identifying and Reconciling Controversies, Trends Mol Med 27 (4) (2021) 314–331.

[56] B.D. Chithrani, A.A. Ghazani, W.C.W. Chan, Determining the Size and Shape Dependence of Gold Nanoparticle Uptake into Mammalian Cells, Nano Lett. 6 (4) (2006) 662–668.

[57] Park, K. S.; Ni, Z.; Côté, A. P.; Choi, J. Y.; Huang, R.; Uribe-Romo, F. J.; Chae, H. K.; O'Keeffe, M.; Yaghi, O. M., Exceptional chemical and thermal stability of zeolitic imidazolate frameworks. *Proceedings of the National Academy of Sciences* **2006**, *103* (27), 10186-10191.

[58] M.A. Luzuriaga, C.E. Benjamin, M.W. Gaertner, H. Lee, F.C. Herbert, S. Mallick, J.J. Gassensmith, ZIF-8 degrades in cell media, serum, and some—but not all—common laboratory buffers, Supramol. Chem. 31 (8) (2019) 485–490.

[59] B. Sha, W. Gao, S. Wang, F. Xu, T. Lu, Cytotoxicity of titanium dioxide nanoparticles differs in four liver cells from human and rat, Compos. B Eng. 42 (8) (2011) 2136–2144.

[60] X. Han, R. Gelein, N. Corson, P. Wade-Mercer, J. Jiang, P. Biswas, J.N. Finkelstein, A. Elder, G. Oberdörster, Validation of an LDH assay for assessing nanoparticle toxicity, Toxicology 287 (1–3) (2011) 99–104.

[61] D. Kota, L. Kang, A. Rickel, J. Liu, S. Smith, Z. Hong, C. Wang, Low doses of zeolitic imidazolate framework-8 nanoparticles alter the actin organization and contractility of vascular smooth muscle cells, J. Hazard. Mater. 414 (2021) 125514.

[62] S. Veeranarayanan, A.C. Poulose, S. Mohamed, A. Aravind, Y. Nagaoka, Y. Yoshida, T. Maekawa, D.S. Kumar, FITC labeled silica nanoparticles as efficient cell tags: uptake and photostability study in endothelial cells, J Fluoresc 22 (2) (2012) 537–548.

[63] J.A.G. McKenzie, A.J. Ridley, Roles of Rho/ROCK and MLCK in TNF-α-induced changes in endothelial morphology and permeability, J. Cell. Physiol. 213 (1) (2007) 221–228.

[64] M.-J. Rabiet, J.-L. Plantier, Y. Rival, Y. Genoux, M.-G. Lampugnani, E. Dejana, Thrombin-Induced Increase in Endothelial Permeability Is Associated With Changes in Cell-to-Cell Junction Organization, Arterioscler. Thromb. Vasc. Biol. 16 (3) (1996) 488–496.

[65] A. Kása, C. Csortos, A.D. Verin, Cytoskeletal mechanisms regulating vascular endothelial barrier function in response to acute lung injury, Tissue barriers 3 (1–2) (2015) e974448–e.

[66] E.S. Harris, W.J. Nelson, VE-cadherin: at the front, center, and sides of endothelial cell organization and function, Curr Opin Cell Biol 22 (5) (2010) 651–658.

[67] M.I. Setyawati, C.Y. Tay, S.L. Chia, S.L. Goh, W. Fang, M.J. Neo, H.C. Chong, S.M. Tan, S.C.J. Loo, K.W. Ng, J.P. Xie, C.N. Ong, N.S. Tan, D.T. Leong, Titanium dioxide nanomaterials cause endothelial cell leakiness by disrupting the homophilic interaction of VE–cadherin, Nat. Commun. 4 (1) (2013) 1673.

[68] M.I. Setyawati, C.Y. Tay, B.H. Bay, D.T. Leong, Gold Nanoparticles Induced Endothelial Leakiness Depends on Particle Size and Endothelial Cell Origin, ACS Nano 11 (5) (2017) 5020–5030.

[69] D. Mehta, A.B. Malik, Signaling mechanisms regulating endothelial permeability, Physiol. Rev. 86 (1) (2006) 279–367.

[70] C. Rüffer, A. Strey, A. Janning, K.S. Kim, V. Gerke, Cell-cell junctions of dermal microvascular endothelial cells contain tight and adherens junction proteins in spatial proximity, Biochemistry 43 (18) (2004) 5360–5369.

[71] E. Dejana, Endothelial cell–cell junctions: happy together, Nat. Rev. Mol. Cell Biol. 5 (4) (2004) 261–270.

[72] A.C. Dumitru, M.A. Poncin, L. Conrard, Y.F. Dufrêne, D. Tyteca, D. Alsteens, Nanoscale membrane architecture of healthy and pathological red blood cells, Nanoscale Horiz. 3 (3) (2018) 293–304.

[73] R. Garcia, Nanomechanical mapping of soft materials with the atomic force microscope: methods, theory and applications, Chem. Soc. Rev. 49 (16) (2020) 5850–5884.
[74] D. Alsteens, R. Newton, R. Schubert, D. Martinez-Martin, M. Delguste, B. Roska, D.J. Müller, Nanomechanical mapping of first binding steps of a virus to animal cells, Nat. Nanotechnol. 12 (2) (2017) 177–183.
[75] A. Calzado-Martín, M. Encinar, J. Tamayo, M. Calleja, A. San Paulo, Effect of Actin Organization on the Stiffness of Living Breast Cancer Cells Revealed by Peak-Force Modulation Atomic Force Microscopy, ACS Nano 10 (3) (2016) 3365–3374.
[76] J. Liu, S. Smith, C. Wang, Reversing the Epithelial-Mesenchymal Transition in Metastatic Cancer Cells Using CD146-Targeted Black Phosphorus Nanosheets and a Mild Photothermal Treatment, ACS Nano 16 (2) (2022) 3208–3220.
[77] J. Liu, L. Kang, S. Smith, C. Wang, Transmembrane MUC18 Targeted Polydopamine Nanoparticles and a Mild Photothermal Effect Synergistically Disrupt Actin Cytoskeleton and Migration of Cancer Cells, Nano Lett. 21 (22) (2021) 9609–9618.
[78] H.J. Sanyour, N. Li, A.P. Rickel, J.D. Childs, C.N. Kinser, Z. Hong, Membrane cholesterol and substrate stiffness co-ordinate to induce the remodelling of the cytoskeleton and the alteration in the biomechanics of vascular smooth muscle cells, Cardiovasc Res 115 (8) (2019) 1369–1380.
[79] H.J. Sanyour, N. Li, A.P. Rickel, H.M. Torres, R.H. Anderson, M.R. Miles, J.D. Childs, K.R. Francis, J. Tao, Z. Hong, Statin-mediated cholesterol depletion exerts coordinated effects on the alterations in rat vascular smooth muscle cell biomechanics and migration, J. Physiol. 598 (8) (2020) 1505–1522.
[80] Fish, K. N., Total internal reflection fluorescence (TIRF) microscopy. *Current protocols in cytometry* **2009,** *Chapter 12*, Unit12.18-Unit12.18.
[81] M.J. Rust, M. Bates, X. Zhuang, Sub-diffraction-limit imaging by stochastic optical reconstruction microscopy (STORM), Nat. Methods 3 (10) (2006) 793–796.
[82] S. van de Linde, A. Löschberger, T. Klein, M. Heidbreder, S. Wolter, M. Heilemann, M. Sauer, Direct stochastic optical reconstruction microscopy with standard fluorescent probes, Nat. Protoc. 6 (7) (2011) 991–1009.
[83] G.T. Dempsey, J.C. Vaughan, K.H. Chen, M. Bates, X. Zhuang, Evaluation of fluorophores for optimal performance in localization-based super-resolution imaging, Nat. Methods 8 (12) (2011) 1027–1036.
[84] Xu, J.; Ma, H.; Liu, Y., Stochastic Optical Reconstruction Microscopy (STORM). *Current Protocols in Cytometry* **2017,** *81* (1), 12.46.1-12.46.27.
[85] P.P. Fu, Q. Xia, H.-M. Hwang, P.C. Ray, H. Yu, Mechanisms of nanotoxicity: Generation of reactive oxygen species, J. Food Drug Anal. 22 (1) (2014) 64–75.
[86] Q. Xu, L.P. Huff, M. Fujii, K.K. Griendling, Redox regulation of the actin cytoskeleton and its role in the vascular system, Free Radic. Biol. Med. 109 (2017) 84–107.
[87] D. Mateo, P. Morales, A. Ávalos, A.I. Haza, Oxidative stress contributes to gold nanoparticle-induced cytotoxicity in human tumor cells, Toxicol Mech Methods 24 (3) (2014) 161–172.
[88] Schlinkert, P.; Casals, E.; Boyles, M.; Tischler, U.; Hornig, E.; Tran, N.; Zhao, J.; Himly, M.; Riediker, M.; Oostingh, G. J.; Puntes, V.; Duschl, A., The oxidative potential of differently charged silver and gold nanoparticles on three human lung epithelial cell types. *Journal of nanobiotechnology* **2015,** *13*, 1-1.
[89] A. Sasidharan, P. Chandran, D. Menon, S. Raman, S. Nair, M. Koyakutty, Rapid dissolution of ZnO nanocrystals in acidic cancer microenvironment leading to preferential apoptosis, Nanoscale 3 (9) (2011) 3657–3669.
[90] A. Manke, L. Wang, Y. Rojanasakul, Mechanisms of Nanoparticle-Induced Oxidative Stress and Toxicity, Biomed Res. Int. 2013 (2013) 942916.
[91] X. Jiang, Y. Wu, P. Gray, J. Zheng, G. Cao, H. Zhang, X. Zhang, M. Boudreau, T.R. Croley, C. Chen, J.-J. Yin, Influence of gastrointestinal environment on free radical generation of silver nanoparticles and implications for their cytotoxicity, NanoImpact 10 (2018) 144–152.
[92] X. Jiang, L. Wang, Y. Ji, J. Tang, X. Tian, M. Cao, J. Li, S. Bi, X. Wu, C. Chen, J.-J. Yin, Interference of Steroidogenesis by Gold Nanorod Core/Silver Shell Nanostructures: Implications for Reproductive Toxicity of Silver Nanomaterials, Small 13 (10) (2017) 1602855.
[93] L.K. Doolittle, M.K. Rosen, S.B. Padrick, Measurement and analysis of in vitro actin polymerization. *Methods in molecular biology* 1046 (2013) 273–293.
[94] W. Gu, X. Bai, K. Ren, X. Zhao, S. Xia, J. Zhang, Y. Qin, R. Lei, K. Chen, Y.-N. Chang, L. Zeng, J. Li, G. Xing, Mono-fullerenols modulating cell stiffness by perturbing actin bundling, Nanoscale 10 (4) (2018) 1750–1758.
[95] S. Sharma, E.E. Grintsevich, M.L. Phillips, E. Reisler, J.K. Gimzewski, Atomic Force Microscopy Reveals Drebrin Induced Remodeling of F-Actin with Subnanometer Resolution, Nano Lett. 11 (2) (2011) 825–827.
[96] Chou Steven, Z.; Pollard Thomas, D., Mechanism of actin polymerization revealed by cryo-EM structures of actin filaments with three different bound nucleotides. *Proceedings of the National Academy of Sciences* **2019,** *116* (10), 4265-4274.
[97] T. Hohmann, F. Dehghani, The Cytoskeleton-A Complex Interacting Meshwork. *Cells* 8 (2019) 4.
[98] H. Strzelecka-Gołaszewska, E. Pròchniewicz, W. Drabikowski, Interaction of actin with divalent cations. 2. Characterization of protein-metal complexes, Eur. J. Biochem. 88 (1) (1978) 229–237.
[99] M.F. Carlier, C. Valentin-Ranc, C. Combeau, S. Fievez, D. Pantoloni, Actin polymerization: regulation by divalent metal ion and nucleotide binding, ATP hydrolysis and binding of myosin, Advances in Experimental Medicine and Biology 358 (1994) 71–81.
[100] W. Brieher, Mechanisms of actin disassembly, Mol. Biol. Cell 24 (15) (2013) 2299–2302.
[101] K. Dong, Z. Wang, Y. Zhang, J. Ren, X. Qu, Metal-Organic Framework-Based Nanoplatform for Intracellular Environment-Responsive Endo/Lysosomal Escape and Enhanced Cancer Therapy, ACS Appl. Mater. Interfaces 10 (38) (2018) 31998–32005.
[102] M. Xu, Y. Hu, W. Ding, F. Li, J. Lin, M. Wu, J. Wu, L.-P. Wen, B. Qiu, P.-F. Wei, P. Li, Rationally designed rapamycin-encapsulated ZIF-8 nanosystem for overcoming chemotherapy resistance, Biomaterials 258 (2020) 120308.
[103] M.A. Luzuriaga, F.C. Herbert, O.R. Brohlin, J. Gadhvi, T. Howlett, A. Shahrivarkevishahi, Y.H. Wijesundara, S. Venkitapathi, K. Veera, R. Ehrman, C.E. Benjamin, S. Popal, M.D. Burton, M.A. Ingersoll, N.J. De Nisco, J.J. Gassensmith, Metal-Organic Framework Encapsulated Whole-Cell Vaccines Enhance Humoral Immunity against Bacterial Infection, ACS Nano 15 (11) (2021) 17426–17438.
[104] Ichiki, T.; Izumi, R.; Cataliotti, A.; Larsen, A. M.; Sandberg, S. M.; Burnett, J. C., Jr., Endothelial permeability in vitro and in vivo: protective actions of ANP and omapatrilat in experimental atherosclerosis. *Peptides* **2013,** *48*, 21-6.
[105] I.M. Kennedy, D. Wilson, A.I. Barakat, Uptake and inflammatory effects of nanoparticles in a human vascular endothelial cell line, Research report (Health Effects Institute) 136 (2009) 3–32.
[106] F. Peng, M.I. Setyawati, J.K. Tee, X. Ding, J. Wang, M.E. Nga, H.K. Ho, D.T. Leong, Nanoparticles promote in vivo breast cancer cell intravasation and extravasation by inducing endothelial leakiness, Nat. Nanotechnol. 14 (3) (2019) 279–286.
[107] W.J. Karlon, P.P. Hsu, S. Li, S. Chien, A.D. McCulloch, J.H. Omens, Measurement of orientation and distribution of cellular alignment and cytoskeletal organization, Ann. Biomed. Eng. 27 (6) (1999) 712–720.